A robust memristive system based on fullerene and HATNA functionalised glycol ethers

M.L.A. Blok

Research Group: Hybrid Materials for Opto-Electronics

Head Supervisor: C. Nijhuis

Daily supervisor: A. Borrini

Abstract

Redox active molecular junctions have shown potential to achieve neuromorphic computing architecture which circumvents the von Neumann bottleneck, delivering memory and rectification properties. Here, to address the limited switching speed and humidity dependence of such molecular switches, the integration of a proton donor in the junction was attempted. However, this was plagued by stability issues regarding the thiol based molecules and their self-assembled monolayers. Therefore, a fullerene and glycol ether based system was investigated, resulting in a system with similar hysteretic properties, high junction yields (89.7%), rectification ratios of 2*10^3. Additionally, the stability of PTEG-1 monolayers and the HATNA-TEG molecules suggests these assemblies could retain functionality in ambient conditions for extended periods of time.

Landscape analysis

In recent years, advancements in Artificial Intelligence (AI) have been unprecedentedly rapid[1]. This is the case for both pre-trained models, such as the well-known Generative Pretrained Transformer (GPT) series[1], and Machine Learning (ML) algorithms which exhibit continual learning[2][3]. Especially the GPT series has seen a boom in popularity due to its impressive capabilities[1]. These developments are accompanied by exponential increases in required computational capacity during training[2]. This raises an issue, many applications of ML algorithms require rapid transfer of data between components which process and store data[4]. When performing
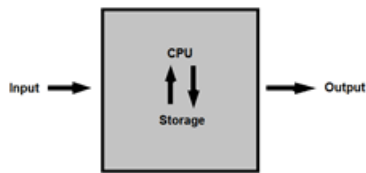
Figure 1: Simplified diagram of Von Neumann architecture, by author.

ML on traditional Von Neumann computer architecture (Figure 1) this transport becomes the rate limiting step, severely hampering the efficiency of the computational system[4]. This issue is known as the Von Neumann bottleneck (VNb) and in some applications of ML this data transfer can take up to 90%[4] of the processing time, meaning that the CPU's computational power cannot be fully utilized. The combination of the VNb and an apparent slowing in Moore's law[5] might indicate that conventional complementary metal oxide semiconductor (CMOS) transistor based computer architecture will not be able to keep up with advances in AI and ML[4]. Therefore, alternative approaches merit investigation. Non-Von-Neumann approaches commonly rely on on memristors, which can be described as a device whose conductance is altered by applied charge, effectively retaining information about previously applied charge[2]. Thus, eliminating the need for additional data transfer. Therefore, this approach allows for circumvention of the VNb. There is considerable ongoing research into the creation of memristive circuits with conventional CMOS hardware[3]. One of these approaches is processing in memory (PIM), essentially this can be conceived as a solution where the basic units of a computer contain memory and processing in the same location[3]. However, there are also a variety of techniques that do not involve CMOS at all, of which neuromorphic computing is one of the most promising[6]. In neuromorphic computing the design of the memristive component is heavily inspired by the synapse and its synaptic gap[7]. This type of memristor has been shown to behave similar to biological synapses, next to displaying Pavlovian learning and having the ability to emulate all the principal logic gates necessary for ML operations[7].

However, to be widely applicable in AI operations, they require much higher switching speeds, which are now on the order of seconds[7], compared to nanoseconds or less in CMOS architecture. Additionally, issues with long term stability, high switching energies and scalability need to be addressed[6]. Possible pathways towards a significant increase in switching speeds, as well as potential improvements to stability and scalability will be investigated in this research project. In a broader sense, due to limitations to CMOS transistor based technology, non-Von-Neumann architecture is necessary for advancement outside of the field of AI and ML, as the physical limit for transistor size is approached[5].

Fundamental Literature

Neuromorphic computing approaches which take inspiration from organic computational units can be divided into two broad categories. The first one is direct modulation of a conductive pathway, through the growth of a conductive filament between two poles[6]. The second one uses redox reactions to modulate conductance, either by driving electrons from one component to another, or interaction with a secondary medium[6]. Filament forming devices allow for a large range of conductance states, but suffer from two influential drawbacks. Although highly tunable, the high write noise causes unpredictability[6]. Moreover, reconfiguration energies are high, as resetting involves induced deconstruction of the filament[6]. On the other hand, neuromorphic computing based on redox reaction driven devices seem to overcome these issues. Different architectures have been explored for these devices such as two or three terminal devices. Two terminal devices contain a top and bottom electrode, where a current applied over the device directly modifies the redox state of an electrolyte and polymer in between, modulating the conductance between electrodes[6]. Alternatively, three terminal devices contain a gate terminal next to a source and drain. A potential applied to the gate terminal changes the conductance between source and drain[6], thus requiring a secondary signal input. To scale these architectures, the challenge is to improve state retention since redox reaction reverses while a potential is not applied and to achieve multiple stages of conductance states while keeping switching energy low[6]. An interesting approach in the redox category consists of a neuromorphic memristive device developed by Wang, Y. et al. (2022). The novelty of this device is its reliance on spike timing dependent plasticity (STDP)[7]. Essentially, STDP describes a systems capability to modulate its output pulse based on the timing of its input pulse with regards to the previous output pulse[6]. In the device
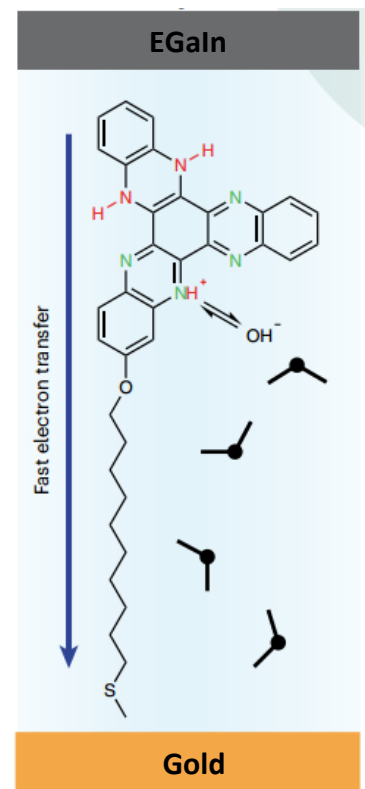
Figure 2: Diagram of HATNA SAM in oxidation state n=2, adapted from Wang, Y. et al.

constructed by Wang, Y. et al. (2022) the functionality originates from the properties of 5,6,11,12,17,18-hexaazatrinaphthylene (HATNA). This molecule contains 6 nitrogen atoms which can each be protonated to form covalent N-H bonds. Protonation of up to two of these sites allows for fast transfer of electrons over the molecule, while subsequent protonation of the following sites reduced conductance of the molecule[7]. This principle allows the device to exhibit its memristive function, effectively retaining a memory of the previous electric pulses. Thus retaining a history of a previous informational state. Progression of protonation allows for oxidation of the HATNA molecule to states containing lower amounts of protons. A full reset could be guaranteed by application of a voltage in opposite direction, converting the molecule back to its n=0 (no coupled protons) oxidation state[7]. The memristive device consists of two electrodes sandwiching, a thiol terminated HATNA moiety (see Figure 2). As thiol groups covalently bind to gold this molecule can be used to construct a self-assembled monolayer (SAM) on top of a gold electrode. The top electrode consists of a layer of Eutectic Gallium-Indium (EGaIn) laid on top, suspended from a syringe[9], whereas the proton donor consists of water present in the atmosphere. The full construction as demonstrated by Wang, Y. et al. (2022) is shown in figure 2. Impressively, the switching and demonstrated synaptic functionality all occurs within the only 2.4nm thick SAM[7]. This construction gives rise to a set of issues regarding stability and switching speed. The proton donor, which consists of water contained within the ambient air is the main contributor. Unfortunately, moisture dependent device performances are quite a limitation for system scalability[7]. Therefore, it was investigated whether these issues can be circumvented by incorporation of a proton source in the SAM.

Focal Point and Research method

In this thesis mercaptoundecanoic acid will be investigated as a possible proton source for the HATNA SAM, by integrating it into the monolayer. This will be done in two ways. The first one, the coabsorption method, where mercaptoundecanoic
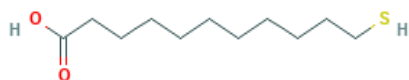
Figure 3: 11-Mercaptoundecanoic acid, from [8]

acid is mixed with HATNA in THF solution. After that, template stripped gold surfaces will be immersed in this solution and incubated overnight. The second method is backfilling which consists of formation of the HATNA monolayer, after which the HATNA monolayer is immersed in a solution of mercaptoundecanoic acid, which then self assembles into the gaps, defects and grain boundaries of the HATNA SAM. Because of the presence of COOH groups, the speed of proton diffusion should be increased, therefore increasing switching speed[7]. The research question is formulated as: ***What are the effects of adding mercaptoundecanoic acid to a HATNA SAM based memristive on its performance?***

This formulation allows for the creation of three sub-questions.

1. *What is the effect of forming the monolayer by coabsorption of mercaptoundecanoic acid on the device's switching speed?*
2. *What is the effect of using backfilling to integrate mercaptoundecanoic acid on the device's switching speed?*
3. *How will modification of the HATNA SAM based device by backfilling and coabsorption of mercaptoundecanoic acid affect its synaptic functionality?*
4. *How is the performance of the modified SAM's affected by humidity?*

Monolayers will be created with pure HATNA and with various concentrations of added mercaptoundecanoic acid, through both the backfilling and coabsorption processes. Additionally, a few samples with only mercaptoundecanoic acid will be made as a comparative standard. Surface characterization will consist of contact angle measurements, AFM and XPS. Performance of the junctions will be investigated through the EGaIn method. The redox behaviour will be further investigated by CV (Cyclic Voltammetry). Based on the described literature three rudimentary hypotheses can be constructed. Firstly; The increase in proton availability in the direct surrounding of the HATNA SAM will lead to an increase in switching speed, as proton diffusion is the rate limiting step[7]. As CMOS architecture operates with switching speeds in the nanoseconds or even faster, it is not expected that the HATNA switch will manage to approach CMOS architecture performance. Secondly; As long as proton diffusion speed remains the rate limiting step, full functionality will be retained and only the time scales will be affected. Thirdly, as mercaptoundecanoic acid will most likely become the dominant proton source, dependency on humidity should decrease significantly. With the research questions fully developed, the fundamentals on which this paper will be written are available. After the theoretical section of this study, the rudimentary hypotheses will be reformulated into more specific hypotheses, as guided by the acquired knowledge. Then follow the detailed experimental method, results, their analysis, and the confirmation or rejection of the polished hypotheses in the discussion and conclusion.

Experimental Method (for in thesis)

11-Mercaptodecanoic acid is obtained from sigma Aldrich and stored in the fridge, HATNA was synthesized and purified by A. Borrini and stored at -80°C under argon.

Template stripping

The gold electrode was prepared by template stripping. First, 200nm Au films were deposited on silicon wafers with a Shen Yang Ke Yi thermal evaporator. Then clean glass slides were glued onto the surface with EPOTEK 353ND, after which the thermal glue was cured at 80C for 3h. These wafers were stored in a N_2 atmosphere low humidity chamber and template stripped immediately before use[7].

Monolayer formation

HATNA monolayers are made by self-assembly on template stripped gold. Solutions for the formation of monolayers are prepared under nitrogen atmosphere in a glovebox kept <10ppm oxygen. HATNA is dissolved in freshly distilled oxygen-free THF to achieve a 0.5mM solution. For the coabsorption process, a stock solution of 0.2mM 11-mercaptodecanoic in THF is made, which is then used to create the three stock solutions of 100, 200 and 300 μM. The HATNA solution receives 50μL 40% NH3(aq) for every 4 mL of solution, so 12.5μL per mL, and is sonicated to achieve full dissolution. Clean vials for the growing of the monolayer are prepared by adding into each 1 mL of HATNA stock solution and 50μL of their respective mercaptoundecanoic diluted stock solution for the coabsorption process. Gold is template stripped when all solutions are ready and immediately submerged in the solution. Vials are capped and left in the glovebox overnight. The next day, the samples are removed from the glovebox and vial, suspended in a funnel and washed with copious amounts of fresh THF, after which they are dried under N_2 and stored in a humidity controlled nitrogen chamber.

Contact angle measurements

Contact angle measurements are performed on the samples with the help of a Krüss Drop Shape Analyzer 30E. At least 3 measurements are made on each sample. The period between droplet deposition and measurement is taken as 5 seconds.

EGaIn measurements

Voltage and current measurements are performed with the EGaIn method. Cone shaped tips of EGaIn/Ga$_2$O$_3$ were used to form electrical contacts according to a previously developed procedure[12].Then, the tips were lowered onto the SAM to form a junction with an optimal contact area between 400 and 1000μm^2.[9] These measurements are performed in a custom made humidity chamber at 60%. The flow of dry and wet air is regulated until the humidity chamber stabilises, after which measurements start. Tips are shaped on bare template stripped gold and then moved over to the sample. Measurements consist of 3 scans per junction with a target of 300 scans in total over all samples per condition or category. Every 3 junctions, or when it seems damaged, the tip is remade. For these measurements compliance is set to 0.105A to prevent damage to the sample during shorts, measurements sweep from -2V to 1V with NPLC set to 5. Curves were recorded with a Keithley 6430 source meter in steps of 5mV. Afterwards, the traces were combined using a Gaussian fit and the rectification ratios were determined for each individual curve. Reported as the average with standard deviation.

Results

AFM

The AFM images of template stripped gold (figure 4) indicate a low surface roughness of 0.3nm, which is essential for the formation of well packed layers, as the thioacetate terminated
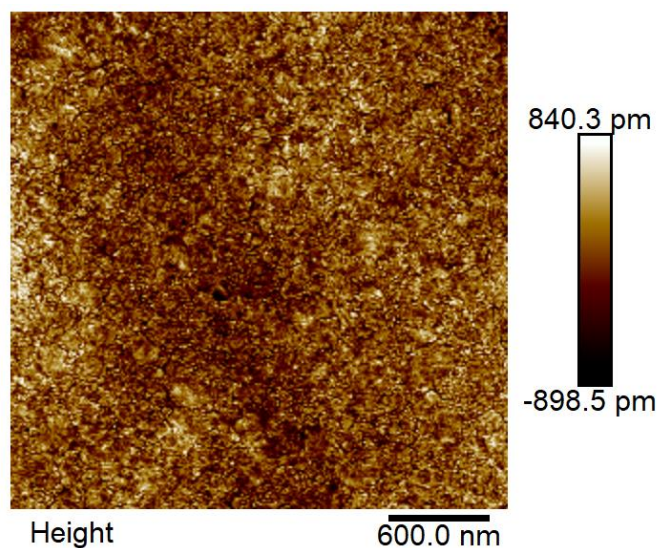
Figure 4: AFM of template stripped gold, with root mean square roughness=0.3nm
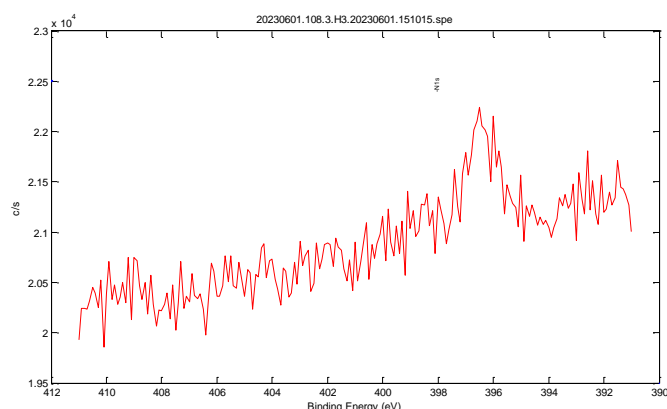
Figure 5: N1s region of XPS on the HATNA-only sample.

C10 chain HATNA is 2.4nm long when assembled on the surface.

XPS

Figure 5 clearly shows that in the N1s region of XPS performed on a sample only containing HATNA, there is only a very weak peak at approximately 396eV. Looking at the signal to noise ratio in this region, the peak is close to undetectable, this finding suggests that the amount of nitrogen present is low

HATNA

Initial results of CA measurements indicate no effect of mercaptoundecanoic acid (C11) coabsorption on CA (table 1). It was hypothesized that the alkyl chain is not long enough, resulting in the COOH moiety not providing any noteworthy hydrogen bonding, due to its distance from the surface and thus not impacting CA. Therefore, samples with mercaptohexadecanoic acid (C16) at 0.5% were prepared, which did not result in any discernible difference either. However, looking at figure 6, it could be possible that the distance between the water on the surface and the carboxylic acid is higher than the typical distance between acceptor and donor in hydrogen bonds (~3A). As the vertical distance in figure 6 is approximately 4.5A, this is quite likely, but packing could still influence the effective distance.
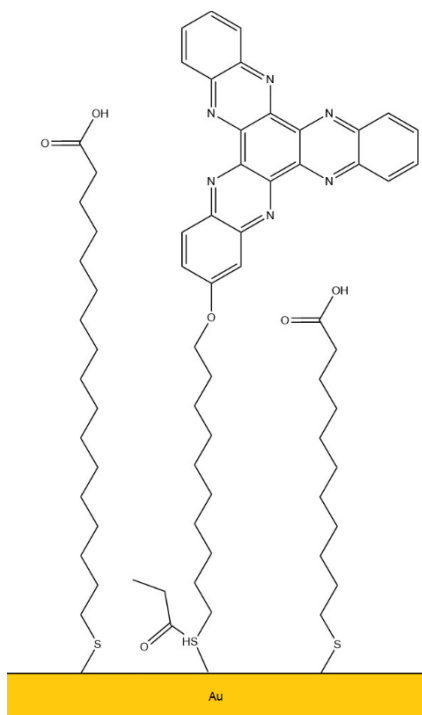
Figure 6: C11, C16 and HATNA –C10 thioacetate on Au

Sample	CA	σ
HATNA	41.12	6
C11 0.1%	37.56	1.98
C11 0.2%	35.63	2.63
C11 0.5%	36.93	0.74
C16 0.5%	35.79	2.49

Table 1: Contact Angles of samples with varying concentrations of C11, C16 compared to HATNA

EGaIn

Measurements with the EGaIn method performed poorly, in the latest samples, none of the J/V curves displayed any form of hysteresis. Additionally, shorts were very common, with 42/70 junctions shorting, giving a poor junction yield of 40%. Because of these findings an NMR was performed on the HATNA that had been used for the all monolayers, confirming that the compound had degraded. After checking every synthesis step and component it was discovered that product 3 and 4 had also degraded in storage, as their presence could no longer be identified by NMR. Ultimately, it turned out that the argon system which had been used to fill every storage container, had not been functioning adequately. This allowed oxygen and potentially other contaminants to react with the products. Thus, after the Argon system was fixed, the synthesis was restarted.

HATNA synthesis

Between reactions, all products are stored in greased and filmed flasks under argon, placed in the fridge at 4C Reactions are also conducted under argon, as both the final and intermediate products are sensitive to oxidation. Figure 7
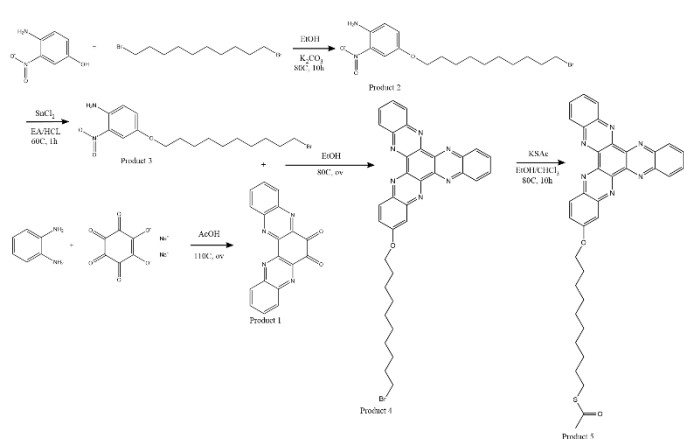
Figure 7: Reaction scheme for the synthesis of HATNA-C10-Thioacetate

includes the entirety of the reaction scheme, the synthesis of individual products is then further discussed in detail

Solvent	T	Time	Additional
CHCl3 :EtOH 1:1	80C	6h	
	80C	Overnight	
DCM: EtOH 1:1	80C	6h	
	80C	6h	5 molar eq. of KI were added to favour exchange of the bromine moiety
DMF	50C	6h	
	50C	6h	

Table 2: Various attempted reaction conditions for synthesis of Product 5

Product 1

600ml of 10% Acetic acid solution is prepared in a 2L round bottom flask and degassed with nitrogen for 20min, after which ortho-phenylenediamine(1.01g, 9.34mmol) is added. Sodium Rhodizonate(1.00g, 4.670) is dissolved in 400ml of water and degassed with nitrogen for 15 minutes, both solutions are then combined and refluxed at 110C under argon overnight. The solution is left to cool to 90C after which 10 ml of concentrated nitric acid(65%) is added for 30 minutes under argon, heated to stay at 90C. The solution is then quenched into 1L of Milli-Q in an ice bath. The product precipitates out and was obtained through vacuum filtration and dried under vacuum afterwards, yielding 1.20g (3.83mmol) of product 1, quinoxalino[2,3-a]phenazine-6,7-dione. H NMR (500 MHz, CDCl3) δ = 8.55 – 8.53 (m, 2H), 8.23 – 8.21 (m, 2H), 7.94 – 7.92 (m, 4H).

Product 2

4-amino-3-nitrophenol(1.00g, 6.49mmol) was added to a 100ml round bottom flask with 1,10-dibromodecane(3.89g, 12.98mmol) and K_2CO_3 (0.897g, 6.49mmol) and dissolved in EtOH. The mixture was refluxed at 80C for 10h and then cooled down to room temperature. Afterwards, the crude reaction mixture was evaporated onto silica and purified in column chromatography with heptane and ethyl acetate(EA) as

eluents. Starting with heptane and slowly switching over to EA. Product 2, 4-((10-bromodecyl)oxy)-2-nitroaniline(1.81g, 4.82mmol), was obtained from the second fraction. 1 H NMR (400 MHz, CDCl3) δ = 7.54 (d, J = 2.9 Hz, 1H, Ph-H), 7.07 (dd, J = 9.1, 2.9 Hz, 1H, Ph-H), 6.75 (d, J = 9.1 Hz, 1H, Ph-H), 5.85 (s, 2H, - NH2), 3.92 (t, J = 6.5 Hz, 2H, -OCH2-), 3.41 (t, J = 6.9 Hz, 2H, - CH2-Br), 1.89 – 1.82 (m, 2H, -CH2-), 1.80 – 1.73 (m, 2H, -CH2-), 1.48 – 1.30 (m, 12H, -(CH2)6-) ppm.

Product 3

Product 2 (0.300g, 0.804mmol) is added to a 50ml round bottom flask with 1ml of concentrated HCL(38%), 5 molar equivalents of SnCl$_2$●2H$_2$O (0.907g,4.020mmol) and 20ml of EA were refluxed at 60C for 1h and then quenched. The solution is then brought to pH 10 by addition of 1M NaOH solution, after which the aqueous layer is extracted thrice with EA. The resulting organic layer is evaporated onto silica and columned with heptane and EA, the product, 4-((10-bromodecyl)oxy)benzene-1,2-diamine, (0.262g, 0.763mmol) was collected from the 3rd fraction. 1 H NMR (400 MHz, DMSO) δ = 6.42 (d, J = 8.3 Hz, 1H, Ph-H), 6.16 (d, J = 2.7 Hz, 1H, Ph-H), 5.96 (dd, J = 8.4, 2.7 Hz, 1H, Ph-H), 4.47 (bs, 4H, -NH2), 3.74 (t, J = 6.6 Hz, 2H, -OCH2-), 3.51 (t, J = 6.7 Hz, 2H, -CH2-Br), 1.78 (p, J = 6.9 Hz, 2H, -CH2-), 1.61 (p, J = 6.8 Hz, 2H, -CH2-), 1.39 –1.20 (m, 12H, -(CH2)6-) ppm

Product 4

Product 3(0.262g, 0.763mmol) and product 1(0.238g, 0.763mmol) are added to a 100ml round bottom flask with 50ml of EtOH and refluxed at 80C overnight, the reaction mixture is then evaporated onto silica and purified in a column with a mixture of heptane and chloroform. Product 4, Br-C10-HATNA (0.165g, 0.266mmol), was obtained from the 2nd fraction. 1 H NMR (400 MHz, CDCl3) δ = 8.58 – 8.45 (m, 4H, Ph-H), 8.34 (d, J = 9.3 Hz, 1H, Ph-H), 7.94 – 7.85 (m, 4H, Ph-H), 7.69 (d, J = 2.7 Hz, 1H, Ph-H), 7.51 (dd, J = 9.3, 2.7 Hz, 1H, Ph-H), 4.14 (t, J = 6.6 Hz, 2H, -OCH2-), 3.35 (t, J = 6.8 Hz, 2H, -CH2-Br), 1.92 – 1.84 (m, 2H, -CH2-), 1.84 – 1.76 (m, 2H, -CH2-), 1.56 – 1.44 (m, 2H,-CH2-), 1.43 – 1.27 (m, 10H, -(CH2)5-) ppm.

Product 5

Product 4(0.160g, 0.258mmol) and 5 molar equivalents of KSAc (0.059g, 0.516mmol) were added to a 100ml round bottom flask with 25ml of chloroform and 25ml of EtOH and left to react for 6h at 80C(reflux). An NMR of the crude reaction mixture already lacked the peak which would indicate the presence of thioacetate on the alkyl chain. After separation by column with CHCl3:Heptane, all obtained fractions contained mostly product 4, whereas the third fraction was contaminated with a very small amount of product 5. Therefore, a variety of reaction conditions was attempted, as displayed in table 2.

None of these conditions yielded any significant amount of product 5 after separation. As the reason for this could not be identified and the amount of time available was limited, this pathway was abandoned.

PTEG-1 and HATNA-TEG

The rapid degradation of the desired HATNA derivative and its intermediate products motivates the search for more stable approaches for the formation of HATNA SAM's. This limited stability in air extends to fully formed monolayers as well, where thiol-metal bonds can be oxidised[10]. Therefore, for effective implementation of HATNA based neuromorphic computing, a robust method for monolayer formation is paramount. X. Qiu et al (2020) demonstrates such a method, where the functional molecules are not bonded covalently to the gold surface, but kept in place by dipole-dipole interactions. This method consists of the formation of a monolayer of PTEG-1, a buckminsterfullerene with a triethylene glycol(TEG) chain. The fullerene chemisorbs onto the metal surface, while the chains can provide a stable framework for other TEG terminated molecules to self-assemble into a bilayer through dipole-dipole interactions[10]. At an estimated 43 kcal/mol bond energy, this bond is stronger than gold-thiol bonds, most favourably estimated at 37 kcal/mol[10]. Thus, the properties of a bilayer consisting of PTEG-1 and a TEG terminated HATNA derivative will be investigated. Depicted in figure 8 is the target bilayer configuration. Due to the TEG chain, PTEG-1 will first form a bilayer on the surface[10], this leads to two hypothetical approaches to form the PTEG-1/HATNA-TEG bilayer. In the first, the bilayer is left intact, then submersed in HATNA-TEG solution, where the difference in concentration will drive replacement of the top layer with HATNA. The second approach involves removal of the top layer by washing with a small quantity of toluene and subsequent treatment with HATNA-TEG. To investigate the viability of the PTEG method as a way to form stable HATNA monolayers for use in neuromorphic computing, it is crucial that the HATNA-TEG retains its memristive properties. These conditions allow for reformulation of the research question: **What is the impact of supporting HATNA-TEG monolayers with SAM's of PTEG-1 by dipole-dipole interaction on its hysteretic behaviour?**

One sub question can also be defined, originating from the two methods: *Which method, PTEG-1 bilayer immersion in HATNA-TEG, or PTEG-1 monolayer immersion in HATNA-TEG, is more suitable for harnessing HATNA's memristive properties?*

X. Qiu et al(2020) conducted molecular junction experiments to determine the conductivity of the PTEG-1 and its stability under loads. This indicated that PTEG-1 is highly conductive and several times more stable than thiol or thioacetate containing

Figure 8: PTEG-1 and HATNA-TEG bilayer on gold.
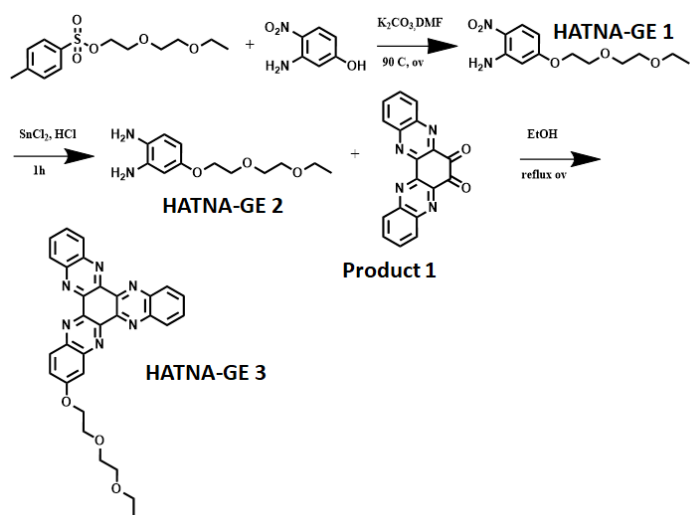
Figure 9 : Reaction scheme for synthesis of HATNA-TEG, obtained from A. Borrini

monolayers. Thus, it is hypothesized that hysteretic behaviour will remain similar, with the added benefit of higher junction stability. Additionally, the direct replacement approach, where the full bilayer is immersed, is hypothesised to yield more consistent results. Because, with the full bilayer present, there are less opportunities for the bottom layer to be damaged or for HATNA to intercalate with the fullerene support.

Synthesis

PTEG-1 was synthesised by the research group of X. Qiu et al (2020). HATNA-TEG was synthesised by A. Borrini according to the reaction scheme in figure 9

In the first step, 2-(2-ethoxyethoxy)ethanol (10.01 ml, 74.5 mmol), DABCO (16.72 g, 149 mmol) and N,N-dimethylpyridin-4-amine (0.911 g, 7.45 mmol) are combined in a round bottom flask and dissolved in 149ml of ice-cold DCM. 4-methylbenzene1-sulfonyl chloride (17.76 g, 93 mmol) is added slowly, the solution is then left to react at room temperature under stirring overnight. Afterwards, the solution is washed with water, 1M of HCL, 1M of KOH and NaCl brine. The obtained organic layer is evaporated under vacuum, yielding 12.15g of 2-(2-ethoxyethoxy)ethyl 4-methylbenzenesulfonate), which was directly used in the next step without further purification.

Subsequent steps are identical to those used for the synthesis of HATNA product 3 and 4 respectively. The product was isolated as a yellow solid in a yield of 87% (0.228 g, 0.440 mmol). ^{1}H NMR (400 MHz, CDCl$_3$) δ 8.71 − 8.58 (m, 5H), 8.51 (d, J = 9.3 Hz, 1H), 8.06 − 7.94 (m, 4H), 7.88 (d, J = 2.8 Hz, 1H), 7.69 (dd, J = 9.4, 2.7 Hz, 1H), 4.43 (dd, J = 5.7, 3.6 Hz, 2H), 4.06 − 4.00 (m, 2H), 3.84 − 3.76 (m, 2H), 3.70 − 3.61 (m, 2H), 3.56 (q, J = 7.0 Hz, 2H), 1.23 (d, J = 14.0 Hz, 3H).

Sample formation

Based on the work of X. Qiu et al (2020) and previous experiments performed by A. Borrini, it was decided to immerse the template stripped gold in 1ml of 0.5mM PTEG-1 solution in toluene for 24h to complete the formation of the bilayer. Thereafter, the samples for the top layer replacement

approach are placed directly in 1ml of 0.5mM HATNA-TEG solution for 5 minutes, rinsed with toluene, dried with N$_2$ and stored. The samples for the monolayer approach are first rinsed with 5-6 drops of toluene, depending on the size of the sample, then immersed in the HATNA-TEG solution for 5 minutes. Afterwards they are rinsed and dried just like the bilayer approach samples. Of both categories, 4 samples were made.

CA PTEG-1+HATNA-TEG

In order to characterise the formed layers, contact angle measurements are performed. These are then compared to values obtained by X.Qiu et al(2020) for PTEG-1, to obtain a rudimentary insight into surface packing and coverage.

Sample	CA(°)	σ_{sd}(°)
PTEG-1 monolayer[10]	45	1
PTEG-1 bilayer[10]	68	1
PTEG-1 + HATNA-TEG mono-approach	58.78	1.85
PTEG-1 + HATNA-TEG bi-approach	62.31	2.79

Table 3: Contact Angles for PTEG-1 mono and bilayers[10] compared to HATNA-TEG systems following mono and bilayer approach

These measurements (Table 3) indicate that neither of the approaches yielded a PTEG-1 mono or bilayer, but that there is HATNA-TEG present on the surface. This is further confirmed by the fact that both approaches yielded very similar contact angles.

EGaIn

Due to limitations to the available time to do measurements, only the properties of the bilayer approach were investigated. Initially, 3 scans were performed per junction, aiming for 400-800 µm^2 junction area, sweeping from -1.5V to 1V. Stability in molecular junctions was low with 56% (52/93) of junctions shorting. However, after elimination of other variables, by cleaning the syringe and filling it with fresh EGaIn, no shorts occurred in 15 junctions. Therefore, a measurement with 10 scans was performed and the voltage sweep was adjusted to -2.5 to 2, yielding a highly stable junction wherein current increased with each scan. Additionally, it was found that junctions with larger areas, 1000-1200 µm^2 gave lower noise ratios and more visible hysteresis, so target junction diameter was adjusted to 35 µm. After these adjustments, junctions were subjected to 20 scans. Due to the larger scan number and wider sweep range, NPLC was set to 3 and tips were remade after every junction. Out of the 24 junctions that were formed, 4 shorted, demonstrating that the system is robust, with a yield of 83% in 20-scan junctions. Including data from 3-scan measurements performed with fresh EGaIn raises this to 89.7%. Figure 10 shows that a high rectification ratio is obtained, at Log(R)=3.25 +- 0.23 and that there is hysteresis
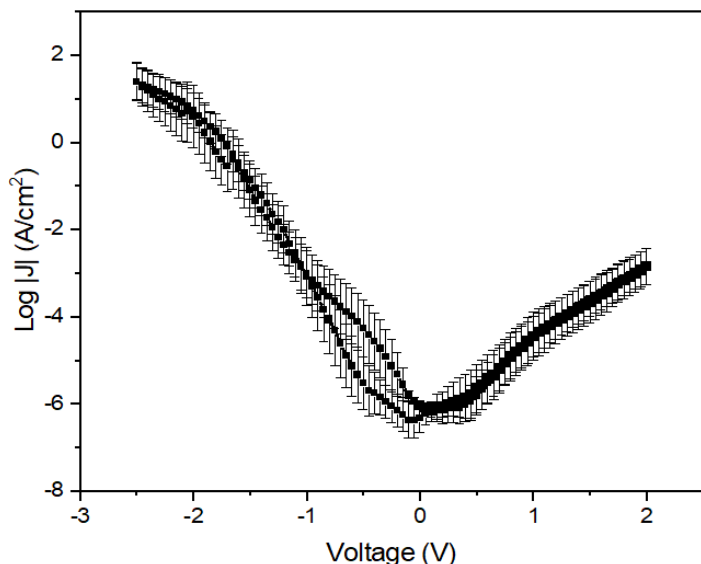
Figure 10: Combined Gaussian fit of 300 scans over 15 bilayer junctions, with split forward and backward curves.
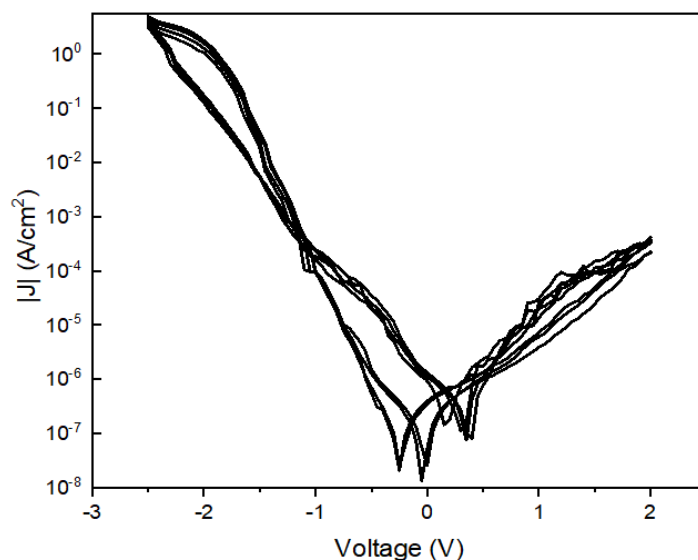
Figure 11: Scan 2,3 and 4 of S3J5, with clear hysteresis inversion occurring at -1.2V.

present. However, the observed hysteresis, between -1V and 0V, is inversed. Individual scans, displayed in figure 11, show both forms of hysteresis.

Discussion & Recommendations

The presence of both hysteresis and a high rectification ratio, together with a junction yield of 86.7% indicates that this system has significant potential to be a more reliable method for HATNA based memristive molecular junctions than reported by Wang, Y. et al. (2022). The replacement of thiol and thioacetate bonds with a fullerene system further supports this claim, as it suggests that these bilayer configurations could remain stable for extended periods of time in ambient air[10]. However, this property should be further investigated.

The reported hysteresis ratio, especially in the positive domain, is much lower than reported by Wang, Y. et al. (2022), 13.7 ± 3.5. However, this is not necessarily a consequence of using PTEG-1 to assemble the bilayer system. Similar curves, including hysteresis inversion, can be observed in thiol based HATNA SAM's[11]. Thus, it can be reasonably concluded that this is an indication of tunable properties by means of variations in the bias window. This explanation consists of partial on-switching occurring while sweeping from positive to negative voltages, followed by partial off-switching at -2.5V. The observed negative hysteresis is then a consequence of partial on-switching occurring around -1.3V while sweeping in the positive direction[11]. Therefore, future research should be conducted to find the optimal bias window resulting in Negative Differential Resistance (NDR) ratios similar to or exceeding those reported by Wang, Y. et al. (2022). Additionally, the applied methods can be further refined, different immersion times for HATNA-TEG should be investigated. This could not only influence the packing density of the surface, but also the level of organisation and orientation. An optimum should be found where the HATNA and PTEG layers most closely resemble figure 8. Therefore,

AFM should also be performed on both the bilayer and monolayer approach to further determine the organisation of the surface. Currently, the mechanism leading to the displayed behaviour, such as the increase of current density over consecutive scans and its subsequent decrease after peaking, usually around the 15th scan, is unknown. Temperature dependent measurements as well as comparisons with models should be conducted in an effort to determine the origin of this rise in current density in future studies. Lastly, The basis for the original research question was well established, but this question could not be answered due to issues with the storage and synthesis of HATNA. Therefore, it is to be recommended that such research is done as soon as a more reliable method for HATNA synthesis is established. However, as HATNA thiols are quite unstable, while the HATNA-TEG shows promise to be very robust, a combination should be considered. This would consist of devising a method to create a mixed top layer, consisting of HATNA-TEG and a TEG-terminated carboxylic acid. Lastly, measurements of the monolayer approach, as initially proposed, should be conducted to determine which of the two approaches yields better performing junctions.

Conclusion

PTEG-1 + HATNA-TEG is a promising system, with a high junction yield of 89.7% and strong indicators that the assembled bilayers could be stable for extended periods of time in ambient conditions. Additionally, a rectification ratio of Log(R)=3.25 +- 0.23 was obtained. This can also be expressed as R=1.78*10^3 Although hysteretic behaviour observed was different from that reported by Wang, Y. et al. (2022), hysteresis inversion and partial on and off switching was also observed in thiol based HATNA SAM's, tunable by adjustment of bias windows. Therefore, it is highly probable that these properties of HATNA remain similar in PTEG-1 + HATNA-TEG systems when compared to thiol based HATNA SAM's. In light of high junction yields and the expected long term stability, PTEG-1+ HATNA-TEG bilayers should be

thoroughly investigated as a robust and reliable method to obtain the properties of HATNA based systems without the pitfalls of thiol oxidation and thiol based SAM instability.

References:

[1]: Zhang, M. & Li, J. A commentary of GPT-3 in MIT Technology Review 2021. *Fundamental Research* **1,** 831–833 (2021).

[2]: Mehonic, A. *et al.* Memristors—from in-memory computing, Deep Learning Acceleration, and spiking neural networks to the future of Neuromorphic and bio-inspired computing. *Advanced Intelligent Systems* **2,** 2000085 (2020).

[3]: Kim, D. *et al.* An overview of processing-in-memory circuits for Artificial Intelligence and machine learning. *IEEE Journal on Emerging and Selected Topics in Circuits and Systems* **12,** 338–353 (2022).

[4]: Mo, P. *et al.* Accurate and efficient molecular dynamics based on machine learning and Non von Neumann architecture. *npj Computational Materials* **8,** (2022).

[5]: The chips are down for Moore's law. *Nature News* Available at: https://www.nature.com/news/the-chips-are-down-for-moore-s-law-1.19338. (Accessed: 18th April 2023)

[6]: van de Burgt, Y., Melianas, A., Keene, S. T., Malliaras, G. & Salleo, A. Organic Electronics for neuromorphic computing. *Nature Electronics* **1,** 386–397 (2018).

[7]: Wang, Y. *et al.* Dynamic molecular switches with hysteretic negative differential conductance emulating synaptic behaviour. *Nature Materials* **21,** 1403–1411 (2022).

[8]: 1.11-mercaptoundecanoic acid. *National Center for Biotechnology Information. PubChem Compound Database* Available at: https://pubchem.ncbi.nlm.nih.gov/compound/11-Mercaptoundecanoic-acid#section=3D-Conformer. (Accessed: 13th July 2023)

[9]: 1.Chen, X., Hu, H., Trasobares, J. & Nijhuis, C. A. Rectification ratio and tunneling decay coefficient depend on the contact geometry revealed by in situ imaging of the formation of Egain Junctions. *ACS Applied Materials & Interfaces* **11,** 21018–21029 (2019).

[10]: 1.Qiu, X. *et al.* Thiol-free self-assembled oligoethylene glycols enable robust air-stable molecular electronics. *Nature Materials* **19,** 330–337 (2020).

[11]: Wang, Y. *et al.* Molecular-Scale In-Operando Reconfigurable Electronic Hardware, Preprint

[12]: 1.Chen, X. *et al.* Molecular diodes with rectification ratios exceeding 105 driven by electrostatic interactions. *Nature Nanotechnology* **12,** 797–803 (2017).